Journal of Materials Chemistry A

ROYAL SOCIETY OF CHEMISTRY

PAPER

View Article Online
View Journal | View Issue

Cite this: J. Mater. Chem. A, 2023, 11, 12266

Layered double hydroxide/boron nitride nanocomposite membranes for efficient separation and photodegradation of water-soluble dyes†

Áine Coogan, [a] Natalia García Doménech,[ab] Donagh Mc Ginley,[a] Tigran Simonian, [acef] Aran Rafferty, [d] Quentin Fedix,[g] Amy Donlon,[a] Valeria Nicolosi [acde] and Yurii K. Gun'ko [*abc]

Widespread access to clean water is becoming increasingly scarce due to various factors, including increasing urbanisation and industrialisation, biodiversity loss, and climate change. The development of innovative and sustainable methods of water purification are urgently required. Herein, we report the development of new, high-performance nanofiltration (NF) membranes based on a recyclable CuAl–CO_3 LDH/BNOx nanocomposite. These membranes have demonstrated up to 100% retention of Evans blue, methyl orange, methylene blue and rhodamine B, and exceptional water flux. Furthermore, the presence of CuAl–CO_3 LDH induces up to 91% photodegradation of these dyes under visible light conditions in 120 minutes using a household LED lamp, acting as a potential low-cost, viable solution to membrane fouling. Importantly, this is the first report of Evans blue degradation by a visible-light active LDH photocatalyst. We believe that this work represents a significant step forward in advanced nanofiltration technology.

Received 15th March 2023
Accepted 24th May 2023

DOI: 10.1039/d3ta01581e

rsc.li/materials-a

1 Introduction

According to a report published by UNICEF and the WHO in 2019, one third of the world's population does not have access to clean, safe drinking water.[1] Dyes, surfactants and heavy metals leached into wastewater from the textile industry are a leading cause of water pollution.[2] The release of these dyes into wastewater streams can have numerous detrimental effects to humans, as well as aquatic flora and fauna. This dye pollution has a significant negative impact on biodiversity in our waterways. The high absorption coefficients of these dyes in the visible light region hinders photosynthesis, as light cannot penetrate the water efficiently.[3] Additionally, many of the dyes used industrially can be carcinogenic and mutagenic, causing long-term damage when ingested by aquatic life, as well as by humans.[4] Azo dyes such as Evans blue are a major concern, with up to 50% of the dye used in the dyeing process being released into wastewater, due to inadequate binding to textiles.[5,6] The toxicity of thiazine and triarylmethane dyes also presents significant risk.[7,8] Innovative methods of water filtration and treatment are therefore urgently needed in order to achieve United Nations Sustainable Development Goal 6 – which is access to clean water for all by 2030. Nanofiltration (NF) is increasingly being explored as an efficient method for water purification.[9,10] NF is typically described as a method of filtration that is capable of rejection of molecules with molecular weights as small as 200 daltons. However, many existing NF membranes suffer from significant, rapid fouling, restricting their lifetime significantly.[11] To contribute to and develop a greener, more circular economy and society, the methods we use for water treatment must be sustainable. Reusable, recyclable NF membranes have the opportunity to be game-changers in this area, and significant research has been conducted in recent years on approaches to anti-fouling and fouling-resistant NF membranes.[12–14]

2D nanomaterials, such as boron nitride, graphene and transition metal dichalcogenides are increasingly being explored as exciting candidates for new NF membranes.[15–18] Exceptional adsorption capacities can be achieved by 2D material-based membranes, due to their high surface-to-volume

[a]School of Chemistry, Trinity College Dublin, Dublin 2, D02 PN40, Ireland. E-mail: igounko@tcd.ie
[b]BiOrbic, Bioeconomy Research Centre, University College Dublin, Belfield, Dublin 4, D04 V1E8, Ireland
[c]AMBER Research Centre, Naughton Institute, Trinity College Dublin, Dublin 2, D02 PN40, Ireland
[d]CRANN Research Centre, Naughton Institute, Trinity College Dublin, Dublin 2, D02 PN40, Ireland
[e]Advanced Microscopy Laboratory, Trinity College Dublin, Dublin 2, D02 PN40, Ireland
[f]Centre for Doctoral Training in the Advanced Characterisation of Materials, AMBER Research Centre, Trinity College Dublin, Dublin 2, D02 PN40, Ireland
[g]Département Chimie Science des Matériaux, Institut Universitaire de Technologie Clermont-Auvergne, 8 Rue Jean-Baptiste Fabre, 43006, Le Puy-en-Velay, France
† Electronic supplementary information (ESI) available. See DOI: https://doi.org/10.1039/d3ta01581e

ratios, allowing more surface area for interaction with contaminants.[19] The stacking of nanosheets when forming membranes results in the formation of nano-porous channels, often allowing for more rapid solvent transport and higher selectivity.[20] Our previous work demonstrated the potential of partially oxidised boron nitride (BNOx) as a nanomaterial for high-performance NF membranes.[21] BNOx can be produced by partial hydroxylation of the edges of BN sheets, which can be achieved by simple thermal oxidation, endowing BNOx with a partially negative surface charge.[22] The introduction of these OH groups has been demonstrated to have no reduction in the NF performance of the exfoliated material when compared with pristine BN. However, the major drawback of these membranes at present is that they are vulnerable to fouling, and must be disposed of after a single use.

Layered double hydroxides (LDHs), often referred to as hydrotalcite-like materials or anionic clays, are layered ionic materials consisting of positively charged metal hydroxide sheets, intercalated with negatively charged counterions. The positive charge in the sheets originates from the doping of divalent M^{2+} species such as Cu^{2+}, Ni^{2+}, Mg^{2+}, and Zn^{2+} with trivalent M^{3+} species such as Al^{3+}, Fe^{3+} and Cr^{3+} in the $M(OH)_2$ matrix, resulting in a partial positive charge.[23] The general formula for a LDH is given by:

$$[M_{1-x}{}^{2+}M_x{}^{3+}(OH)_2]^{x+}[A^{n-}]_{x/n}\cdot mH_2O$$

where A^{n-} represents the intercalating, charge balancing counter-anion, and x is the molar fraction of trivalent cations in the material. Typically, an LDH is successfully synthesised when $0.2 \leq x \leq 0.4$. A wide variety of anions can occupy the interlayer space – the most typical intercalating species being carbonate, nitrate, sulfate, and halide ions.

In recent years, there has been a resurgence in the study of LDHs, owed in part to their semiconductor nature.[24] The use of LDHs can be advantageous over other traditional semiconducting nanomaterials, due to high scalability, low cost and ease of synthesis, as well as high bandgap tunability through variation of the metal cations, as well as the intercalating species.[25] Due to these interesting and unique properties, many recent reports have examined the applications of LDHs in heterogeneous catalysis, specifically as electrocatalysts and photocatalysts.[26–28] In particular, numerous reports of the design of transition-metal based LDHs for photodegradation of dyes in water remediation applications have emerged in recent years.[29,30] Photocatalytically active nanomaterials may represent an innovative route to achieve anti-fouling behaviour in NF membranes. Despite this, to the best of our knowledge, no reports exist of exploiting the photocatalytic activity of LDHs for use as anti-fouling additives in NF membranes.

Herein, we present the development of new, high-performance hybrid CuAl–CO_3 LDH/BNOx NF membranes for efficient separation and visible-light-driven photocatalytic degradation of several dyes – Evans blue, methyl orange, methylene blue and rhodamine B. We believe this innovative route to anti-fouling represents a significant step forward in advanced sustainable nanofiltration research.

2 Experimental

2.1. Starting materials

Hexagonal boron nitride (h-BN) powder was purchased from Merck (particle size = 6–30 mm). Evans blue (EB, ≥75%), methylene blue (MB, ≥82%), rhodamine B base (RhB, 97%), terephthalic acid (TA, 98%) and PERDROGEN™ 30% H_2O_2 (w/w) were purchased from Sigma-Aldrich. Methyl orange (MO, ≥95%) was purchased from VWR International Ltd. Copper nitrate trihydrate ($Cu(NO_3)_2\cdot 3H_2O$, puriss, p.a. 99–104%) and aluminium nitrate nonahydrate ($Al(NO_3)_3\cdot 9H_2O$, ≥98%) were purchased from Honeywell Fluka. Sodium carbonate (Na_2CO_3 99.5%) was purchased from Acros Organics. Sodium hydroxide (NaOH, general purpose grade) was purchased from Fisher Chemical. Millipore Water (MP H_2O) was obtained using an in-house Milli-Q system with resin filters in Trinity College Laboratories. Durapore membrane filter templates (hydrophilic polyvinylidene fluoride, PVDF, with 0.45 μm pore size and 47 mm diameter) were purchased from Merck Millipore Limited. The sonic bath used was Ultrawave model U100H from Ultrawave Ltd. Super premium microscope slides were purchased from VWR. Millipore All-Glass Filter Holder Kit for vacuum filtration was purchased from Merck.

2.2. Instrumentation and characterisation

UV-vis absorption spectra were recorded using an Agilent Cary60 UV-visible spectrophotometer. All measurements were conducted using MP H_2O as solvent. Solid state diffuse reflectance (DR) UV-vis-NIR absorption spectra were recorded using a PerkinElmer Lambda 1050 UV-vis-NIR spectrophotometer with 150 mm InGaAs integrating sphere. Samples were prepared for diffuse reflectance (DR) UV-vis by drop-casting some of the colloidal suspension onto a VWR super premium microscope slide cut to size, followed by solvent evaporation using a hot plate at 100 °C. Zeta potential measurements were carried out using a Malvern Panalytical Zetasizer and disposable folded capillary zeta cells. Fourier transform infrared (FT-IR) spectra were recorded using a PerkinElmer Spectrum 100 FT-IR with diamond UATR accessory. Powder X-ray diffraction (pXRD) was carried out using a zero-background holder and a Bruker D2 Phaser (second gen). Measurements were performed using Cu K_α radiation, and a range of 2θ = 5–80°, with fluorescence correction. Scanning electron microscopy (SEM) images were obtained using a Zeiss Ultra Plus Scanning Electron Microscope. Samples were prepared for SEM by adhering a portion of the membranes to carbon tab-covered cross-section SEM stubs. Mercury porosimetry was performed using an Autoscan-33 Porosimeter (Quantachrome, Hampshire, UK) with a default contact angle of 140°. Samples were prepared for transmission electron microscopy (TEM) *via* drop-casting of dispersed material in water on a 400-mesh lacey carbon Cu TEM grid followed by drying in vacuum overnight. TEM images were obtained using an uncorrected FEI Titan (scanning) transmission electron microscope (accelerating voltage = 300 kV). Spectrum imaging was carried out on the FEI Titan (beam current = approx. 500 pA) using a Bruker Quantax XFlash 6T-30 30 mm^2 energy dispersive X-ray spectroscopy (EDX)

detector and a Gatan Tridium GIF system (for electron energy loss spectroscopy (EELS)). Photoluminescence (PL) emission measurements were performed using a Horiba Jobin Yvon Fluoromax-4 and 10 mm quartz cuvette with 200 nm cut-off. Fluorescence emission spectra were recorded using excitation and emission slits of 2.5 nm, 1 nm increments, and an integration time of 0.1 s.

2.3. Preparation of bulk BNOx

This method was carried out according to our previous report.[21] Bulk h-BN powder (5 g) was partially oxidised in a furnace in air, using a ramp rate of 5 °C, a target temperature of 1000 °C, and was held at the target temperature for 30 min to obtain bulk BNOx powder.

2.4. CuAl–CO_3 LDH synthesis

The synthesis was carried out as described in previous work published by our group, adapted from the synthesis by Berner *et al.*[31,32] Briefly, a co-precipitation was carried out by the dropwise addition of $Cu(NO_3)_2 \cdot 3H_2O$ (1.35 g, 5.58 mmol) and $Al(NO_3)_3 \cdot 9H_2O$ (2.1 g, 5.58 mmol) in 100 mL of MP H_2O to sodium carbonate (0.81 g, 7.5 mmol) in 200 mL of MP H_2O.

Drops of 1 M NaOH were added as required to maintain a pH of around 10. The solution was stirred for 4 h and aged overnight at room temperature (approx. 18–25 °C). The resulting material was cleaned *via* centrifugation (5500 rpm, ×3 MP H_2O) and dried in an oven at 80 °C and ground to obtain a powder.

2.5. LDH/BNOx nanocomposite and membrane preparation

As-prepared CuAl–CO_3 LDH (60 mg) and BNOx (240 mg) were added to a round-bottomed flask with 100 mL of MP H_2O and sonicated for 24 h to obtain the LDH/BNOx nanocomposite. Membranes were prepared by taking 50 mL of the suspension and passing it through a PVDF template (pore size = 0.45 μm, diameter = 47 mm) by vacuum filtration, as described in our previous work.[21]

2.6. Dye retention and water permeance performance testing

Four water soluble dyes were used for testing the retention of the LDH/BNOx nanocomposite-based NF membranes – Evans blue (EB), methyl orange (MO), methylene blue (MB) and rhodamine B (RhB). Aqueous solutions of each dye were prepared to have a UV-vis absorbance at λ_{max} of 1–1.5 a.u., as shown in Table 1.

Table 1 Concentrations and maximum absorbances of the four dyes used for testing membrane NF performance

Dye	λ_{max} (nm)	Abs. (a.u.)	Conc. (μM)
Evans blue	608	1.06	15
Methyl orange	460	1.50	50
Methylene blue	664	1.18	27
Rhodamine B	558	1.49	20

20 mL of the dye solution was passed through the membrane using vacuum filtration operating at a pressure of 1 bar. A UV-vis absorption spectrum of both the feed and the permeate were acquired. The permeate was further concentrated to obtain a 3 mL aliquot using rotary evaporation and re-dissolution to ensure a higher level of accuracy in the calculations, and a UV-vis absorbance spectrum of the concentrated permeate was also obtained. Eqn (1), which is commonly used for NF, and as described in our previous work, was used to calculate the retention:

$$R_x(\%) = \left(1 - \frac{A_{P,\lambda_{max}}}{A_{F,\lambda_{max}}}\right) \times 100 \quad (1)$$

where R_x is the retention in percentage, $A_{F,\lambda_{max}}$ is the absorbance at λ_{max} of the analyte in the feed, and $A_{P,\lambda_{max}}$ is the absorbance at λ_{max} of the analyte in the permeate.

Water permeance measurements in our dead-end filtration system were carried out both for the PVDF template, as well as the LDH/BNOx membrane according to our previous work, using 20 mL of MP H_2O and an operating pressure of 1 bar. Flux was calculated according to eqn (2), as carried out in our previous work[21]

$$F = \frac{V}{At} \quad (2)$$

where F is the flux in L m^{-2} h^{-1}, V is the volume of H_2O in L, A is the working area in m^2, and t is the time taken for the analyte to pass through the membrane (in h). The working area of the fritted glass filtration system is 9.6×10^{-4} m^2.

2.7. Adsorption tests

An as-prepared LDH/BNOx membrane was cut into two, with one half being placed in a clean, polycarbonate Petri dish. 10 mL of the dye solution was added to the Petri dish, and the Petri dish was closed and placed in the dark. Regular aliquots were taken over the course of 6 up to hours for UV-vis analysis and returned to the Petri dish in a timely manner to minimise the light exposure time. The adsorption was modelled using pseudo-second order (PSO) and intra-particle diffusion (IPD) kinetic models, as shown in eqn (3) and (4), respectively.

$$\text{PSO}: \frac{t}{q_t} = \frac{1}{k_2 q_2^2} + \frac{1}{q_2} t \quad (3)$$

$$\text{IPD}: q_t = k_{IPD,i} t^{0.5} + c_i \quad (4)$$

where q_t is the amount adsorbed at time t (in mg g^{-1}), q_2 is the maximum adsorption capacity for the PSO model, k_2 is the apparent PSO rate constant, $k_{IPD,i}$ is the apparent IPD rate constant for a stage i in the IPD process, and c_i is the intercept of the plot of q_t *vs.* $t^{0.5}$ and corresponds to the thickness of the boundary layer. The second half of the membrane was used for the photocatalysis experiments, as described in Section 2.8.

2.8. Photocatalytic degradation testing

An as-prepared LDH/BNOx membrane was cut into two, with one half being placed in a clean, polycarbonate Petri dish. 10 mL of the dye solution was added to the Petri dish, along

with 10 μL of 30% w/w H_2O_2 solution. The open Petri dish was placed under a Parkside (Lidl) 5 W COB LED lamp operating at maximum power for 120 min. Aliquots were taken every 10 min over the course of 120 min for UV-vis analysis and returned to the Petri dish in a timely manner to maximise the light exposure time. The photocatalytic degradation of each dye by the LDH/BNOx membranes was performed in triplicate. The photodegradation process was modelled using pseudo-first order (PFO) degradation kinetics, as described in eqn (5).

$$\text{PFO} : \ln\left(\frac{C_0}{C_t}\right) = k_1 t \quad (5)$$

where C_0 is the initial dye concentration, C_t is the concentration at time t, and k_1 is the apparent PFO rate constant.

2.9. H_2O_2 controls in absence of catalyst

The experiment was performed as described in Section 2.8, with no membrane added as a photocatalyst, to determine the extent of dye photobleaching with H_2O_2 in the presence of visible light.

2.10. Confirmation of hydroxyl radical (·OH) generation

The generation of ·OH radicals by the LDH/BNOx were monitored using the terephthalic acid (TA) probe technique, as reported by Page *et al.*[33] 4 round-bottomed flasks were filled with 10 mg of TA and 50 mL of 20 mM NaOH aqueous solution to aid with aqueous solubility. 30 mg of LDH/BNOx nanocomposite was added to each flask. One flask was placed under the LED lamp, and the second was placed in the dark. To the third and fourth flasks, 20 μL of H_2O_2 (30% (w/w)) was added. One of these was placed under the LED lamp, and the other was placed in the dark. The samples were left for three hours, after which the solids were removed by centrifugation at 15 000 rpm for 2 minutes. The supernatant was retained, and photoluminescence emission spectra of the fluorescent product, hydroxyterephthalic acid (hTA), were obtained using an excitation wavelength of 315 nm and an emission range of 350–500 nm.

3 Results and discussion

3.1. Characterisation of LDH/BNOx nanocomposite material and membranes

BNOx was chosen over BN to fabricate the NF membranes due to the negative surface charge which arises as a consequence of the introduction of –OH groups during the thermal oxidation process, as previously reported by our group.[21] BNOx therefore has the ability to participate in attractive electrostatic interactions with LDHs, and should result in a uniform, electrostatically-stabilised nanocomposite. LDH nanosheets have an intrinsic positive surface charge, due to the doping of M^{3+} species in the $M(OH)_2$ units.[34] CuAl–CO_3 LDH in particular was chosen for this study as it has previously been reported in literature to exhibit photodegradation of azo dyes such as MO, and presents less risk for water treatment than more photoactive Cr-containing LDHs, which can sometimes be prone to oxidative leaching of Cr^{6+}.[35] Zeta potential (ζ) measurements of as-prepared CuAl–CO_3 LDH and exfoliated BNOx were carried out in aqueous solution (pH 7) to confirm the presence of these complementary surface charges, and average values of $\zeta_{BNOx} = -30.7$ mV and $\zeta_{LDH} = +33.6$ mV were obtained (Fig. S.1 and S.2†).

A number of different compositions were tested for the formation of the nanocomposite, the details of which are discussed in Section S.2 of the ESI.† An optimal composition of 20 : 80 LDH/BNOx by mass was determined, as this level of LDH loading should be theoretically high enough to induce photocatalysis, but low enough to maintain the integrity and high performance previously reported for BNOx-based NF membranes. The exfoliated LDH/BNOx nanocomposite was prepared by sonication for 24 h, and the membranes were prepared *via* the common vacuum filtration technique, as described in our previous reports.[10,21] The resulting nanocomposite and membranes were characterised by pXRD, FT-IR, SEM, TEM, HAADF-STEM, EDX, EELS, mercury porosimetry and zeta potential. Fig. 1(a) shows a direct comparison between the pXRD patterns of the two components of the membrane, and the membrane itself. The most prominent reflections observed from the membrane sample are the CuAl–CO_3 LDH (003) reflection at $2\theta = 12.1°$, the BN (002) reflection at $2\theta = 26.8°$, and the $B(OH)_3$ reflection at $2\theta = 28.0°$.[21,32] All observed pXRD reflections in the membrane sample can be indexed to the characteristic reflections of CuAl–CO_3 LDH (JCPDS 46-0099), and BNOx (JCPDS 01-073-2095 for boron nitride, and JCPDS 30-0199 for boric acid ($B(OH)_3$)) – with no formation of any undesirable side products.

FT-IR also was performed on the sample, as shown in Fig. 1(b). The FT-IR spectrum of the membrane contains peaks characteristic of both BNOx and CuAl–CO_3 LDH. The B–N stretch (750 cm^{-1}) and B–N–B bend (1250–1500 cm^{-1}) can be observed, with the B–N–B bend broadening and losing detail due to overlap with the CuAl–CO_3 LDH ν_3 CO_3^{2-} stretch (1350 cm^{-1}). Additionally, there is a broad O–H stretch from roughly 3000–3600 cm^{-1} due to the overlap of the BNOx O–H band at 3000–3200 cm^{-1} and the CuAl–CO_3 LDH O–H stretch centred at 3400 cm^{-1}.[22,36]

Top-view and cross-sectional SEM imaging was conducted to determine the morphological profile of the membranes, as shown in Fig. 2. It is evident from SEM imaging that the membranes exhibit a very uniform, porous profile, with no obvious layering or separation of the two materials observed. Additional top-view and cross-section SEM images are shown in Fig. S.7 in Section S.3 of ESI.† These membranes have a remarkably similar morphological profile to previously reported BNOx membranes, with a calculated mean thickness of 121 ± 8 μm (Fig. S.8†).

From the SEM images, it is apparent that there is a uniform dispersion of larger and smaller nanosheets. Size distribution analysis of the lateral sizes of nanosheets in the membrane structure was performed, revealing a mean lateral size of 0.85 μm and a large standard deviation of 0.38 μm (Fig. S.9†). Furthermore, sheets sampled through size distribution analysis range widely in lateral size from 0.19 to 2.09 μm. This is indicative of a large, broad distribution consisting of smaller

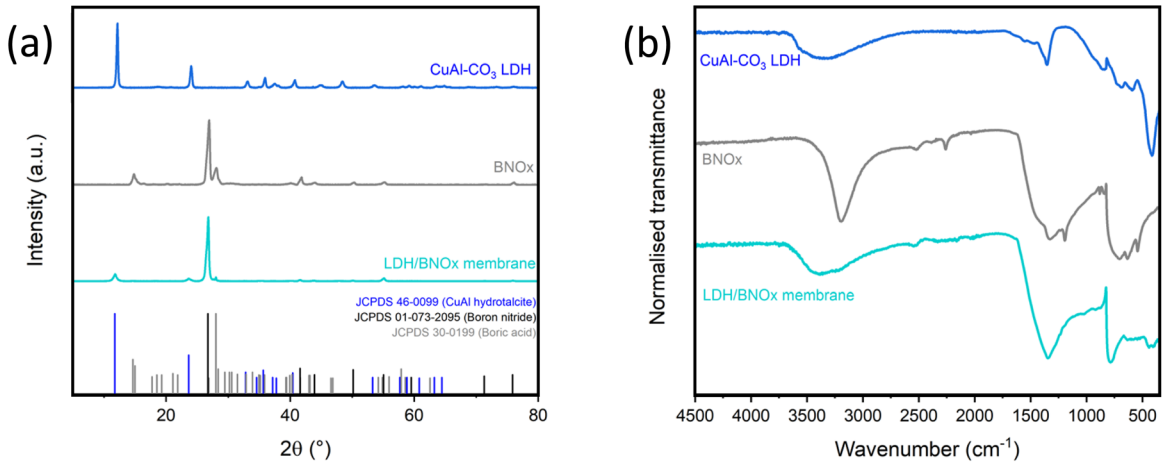

Fig. 1 (a) pXRD patterns and (b) FT-IR spectra of CuAl–CO_3 LDHs (blue), BNOx (grey) and LDH/BNOx nanocomposite (turquoise). pXRD reference patterns are provided for CuAl hydrotalcite, boron nitride and boric acid.

and larger flakes. Additionally, TEM imaging was performed on exfoliated BNOx, and suggests that the larger, irregular rounded flakes present in the membrane are representative of BNOx nanosheets, with an average lateral size of 0.95 ± 0.32 μm, and flake sizes ranging from 0.43 to 1.90 μm. (Fig. S.10 and S.11†). This indicates that a sizable population of smaller sheets in the membrane are representative of CuAl–CO_3 LDH nanosheets, which is in line with expectations based on our previous reports.[32] This broad particle size distribution is an expected consequence of using liquid phase exfoliation in water, without further post-processing steps for size selection.[16,37] To further confirm the composition of the LDH/BNOx nanocomposite, HAADF-STEM was conducted in combination with EDX and EELS mapping, and confirms the presence of both individual CuAl–CO_3 LDH and BNOx nanosheets in the nanocomposite, as shown in Fig. 3.

Mercury porosimetry was conducted on the LDH/BNOx membrane sample to investigate the porosity of the membranes, in the approximate 10 nm to 10 μm range, as shown in Fig. 4. Fig. 4(a) shows the intrusion of mercury into the sample as a function of pore diameter. At initial low pressures, the rate of intrusion is constant. As the pressure builds, mercury is forced into increasingly smaller pores, with an uptake occurring at the 4 μm mark. A gradual filling of pores then occurs to approximately 600 nm. At this point, a second distinct stage of filling is observed, almost linearly, to 150 nm. This region is significant, accounting for approximately 0.25 $cm^3\ g^{-1}$ or 38.5% of the total pore volume (0.65 $cm^3\ g^{-1}$). A third and final stage of filling occurs at 150 nm, with a steep rise in the curve due to rapid intrusion, before gradually plateauing out at 15 nm, with no further intrusion occurring as all pores are fully filled. The resultant pore size distribution, shown in Fig. 4(b), reveals that the vast majority of pores are <1 μm in size. Pores in the 10–200 nm range dominate the material, with a sharp peak at approximately 100 nm indicating a high concentration of pores within a narrow size range. The porosimetry data is in good agreement with the morphologies observed in the SEM images in Fig. 2, where porosity is observed between the flakes. Broadly speaking, there are strong similarities between the LDH/BNOx membranes developed here, and BN and BNOx-based membranes previously developed by our group.[10,21] In particular, a BN membrane exfoliated in *N*-methyl-2-pyrrolidone exhibited a total pore volume of 0.76 $cm^3\ g^{-1}$ and a sharp pore size distribution peak at approximately 100 nm. Like that membrane, we consider the LDH/BNOx membrane

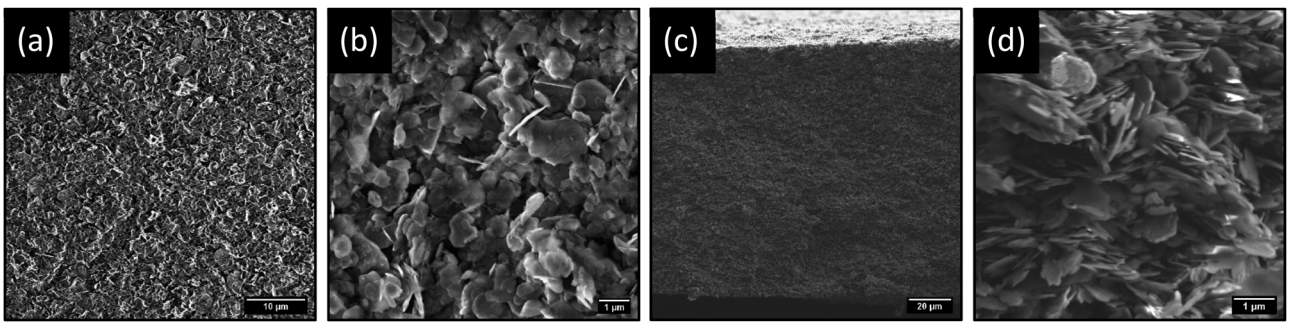

Fig. 2 (a and b) Top-view and (c and d) cross-sectional SEM images of LDH/BNOx membranes. Lower magnification images (a and c) show general uniformity of membranes, and higher magnification (b and d) shows finer membrane structure consisting of networks of nanosheets.

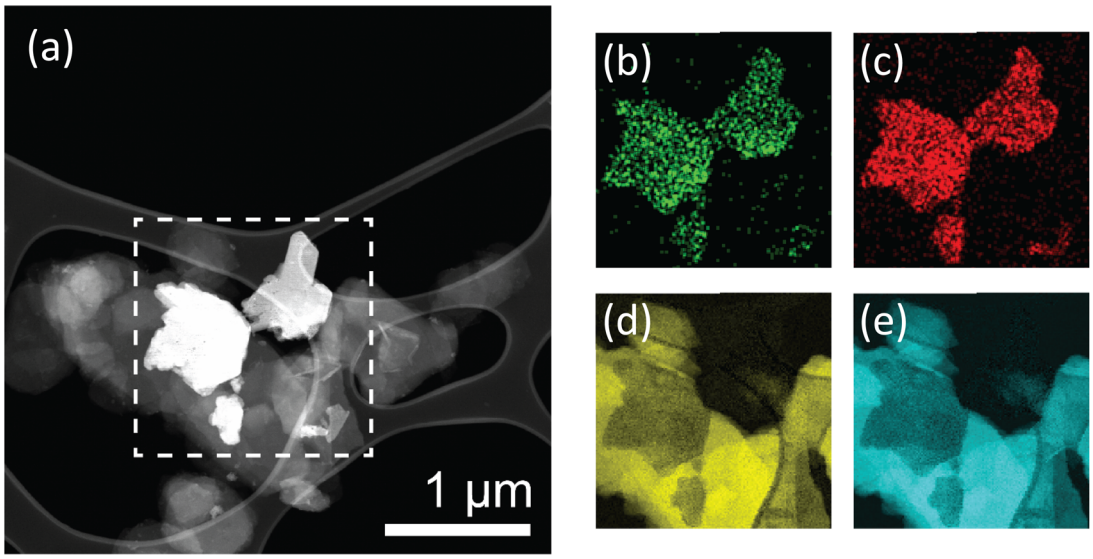

Fig. 3 HAADF-STEM image (a) of LDH/BNOx nanocomposite. Dashed box in (a) is area under analysis in (b)–(e). Elemental mapping of Al (b) and Cu (c) *via* EDX, and N (d) and B (e) *via* EELS. Scale bar in (b)–(e) is same as in (a).

developed here to be a low bulk density material with an open, interconnected porous network.

Thus, the combination of SEM, TEM, and mercury porosimetry confirms that the LDH nanosheets integrate well into the BNOx-based membranes, and therefore should not cause any major differences in NF performance.

3.2. Nanofiltration performance of LDH/BNOx nanocomposite membranes

Once it was confirmed that the LDH/BNOx nanocomposite could produce uniform membranes of similar morphology and pore characteristics to previously reported BN and BNOx membranes, these membranes were assessed for their ability to remove water-soluble dyes from water. Two azo dyes (EB and MO), a triarylmethane dye (RhB) and a thiazine dye (MB) were tested, to examine the ability of the membranes to retain dyes of various sizes, charges (anionic *vs.* cationic) and functional groups. The dye retention performance of the membranes was tested by passing 20 mL aliquots of the dye through the membranes, and examining the difference in absorption of the feed and filtrate solutions, as per previous reports.[10,21] The UV-vis absorption spectra of feeds and samples of permeates of all four dyes are shown in Fig. 5. The absorbance values at λ_{max} for each dye were recorded, and the retentions of each dye were calculated using eqn (1). The average retentions of each dye are shown in Table 2, along with the number of membranes evaluated in each case.

These retention values compare favourably with some of the best in literature for BN/BNOx-based membranes, as well as other 2D material-based membranes.[38,39] For example, amino-functionalised h-BN membranes showed excellent retention for larger molecules such as EB (>99%), and much lower values for smaller molecules such as MB (50.3%) and RhB (58.3%). However, the retention can be greatly improved to 94.1% for MB and >99% for RhB by increasing the membrane thickness.[18] GO membranes have been demonstrated to have dye rejection values of 98.4%, 98.9% and 86.4% for MO, MB and RhB respectively.[40] WS_2-based membranes exhibited retentions of

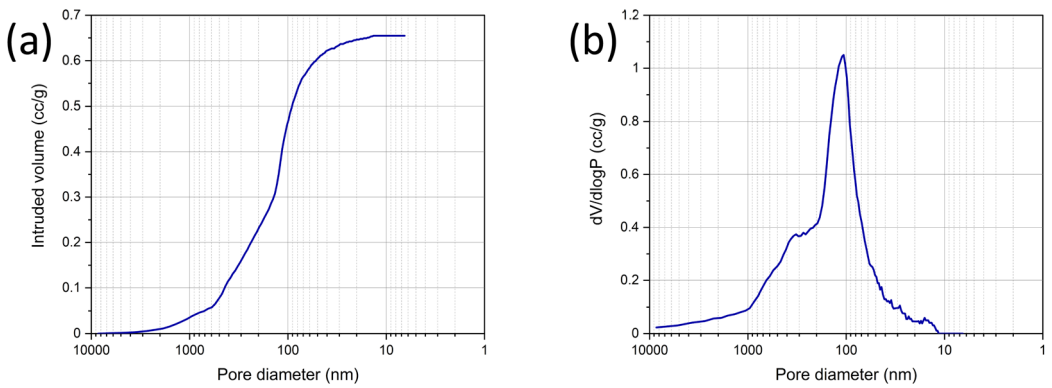

Fig. 4 (a) Mercury intrusion and (b) pore size distribution of the LDH/BNOx membrane sample.

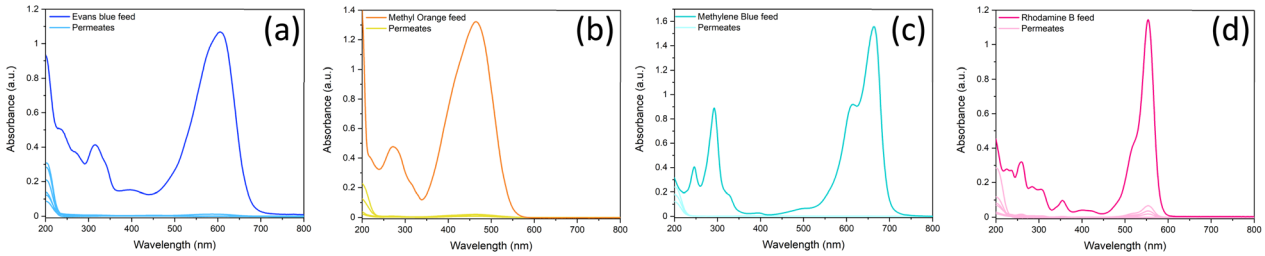

Fig. 5 UV-vis spectra demonstrating the retention of 20 mL of (a) 15 μM Evans blue, (b) 50 μM methyl orange, (c) 27 μM methylene blue, and (d) 20 μM rhodamine B by LDH/BNOx nanocomposite membranes.

Table 2 Mean retention values of LDH/BNOx membranes for a variety of dyes

Dye tested	Mean retention (%)	Number of membranes tested
Evans blue (15 μM)	99.7 ± 0.4	8
Methylene blue (27 μM)	99.9 ± 0.1	5
Methyl orange (50 μM)	96.8 ± 3.1	11
Rhodamine B (20 μM)	97.4 ± 2.1	5

90% for EB.[41] It is therefore evident that the LDH/BNOx membranes reported exhibit exceptional retention for larger dyes such as EB (dimensions: 1.2 nm × 3.1 nm), as well as smaller dyes such as MB (dimensions: 1.4 nm × 0.6 nm), and are in line with some of the best results reported in the literature.

The mechanism of dye removal from water by LDHs generally follows two schemes – incorporation of the dye into the LDH interlayer gallery *via* anion exchange, and dye adsorption to the nanosheet surface.[42] Carbonate-intercalated LDHs typically are the most stable sub-type, as the divalent carbonate anion is held strongly in the LDH interlayer, so adsorption *via* anion exchange in these LDHs is less commonly observed.[43] The dominant adsorption mechanism therefore is likely surface adsorption. LDHs have a positive surface charge, so tend to preferentially adsorb anionic species through electrostatic interactions.

Interestingly, no clear trend can be observed between the charge of the dye and the retention in this case. It can be observed that EB (an anionic dye) and MB (a cationic dye) both exhibit exceptional retention of up to 100%, with marginally lower values obtained for MO (anionic) and RhB (cationic). This serves as further evidence that the introduction of LDHs into BNOx-based NF membranes has no significant impact on the NF performance. Our previous reports on BNOx NF membranes indicates the partial negative surface charge may have a small effect on the retention compared to pristine BN, resulting in marginally higher retention of cationic dyes.[21] However, the dominant retention mechanism observed is likely a result of the BNOx bonding and structure. Hexagonal BN is isostructural to graphene, with sp^2 hybridised alternating B and N atoms in a hexagonal arrangement, resulting in electron delocalisation and a resultant π-system. It has been reported that a major factor in the high retention values and high adsorption capacities of BN and BNOx towards dye molecules is due to π–π interactions.[44,45] It is therefore evident here that BNOx is the material responsible for the high retention values in the LDH/BNOx nanocomposite membranes.

Another key measure of membrane performance is the water flux or permeance. While high retention capacity is a vital property of high-performance water purification membranes, it must be ensured that this does not come at the cost of water transport across the membrane. In order to more accurately assess the suitability of our NF system for water purification, solvent flux studies were carried out on both the LDH/BNOx membranes, as well as the PVDF support (summary in Section S.5 of ESI, Tables S.2 and S.3.†), The hydrophilic PVDF template exhibited low resistance to water flow, as expected, with high flux values of 7360 ± 232 L m^{-2} h^{-1} at an operating pressure of 1 bar. The pure water permeance of the LDH/BNOx membranes on the PVDF support was measured to be 1626 ± 35 L m^{-2} h^{-1}, which is slightly higher than previously reported BNOx membranes (1163 L m^{-2} h^{-1}).[21] The water flux is very high for a membrane of this thickness, when compared with the literature. For example, these membranes exhibit water permeance rates comparable with amino-functionalised h-BN membranes with 0.4 μm thickness (1500 L m^{-2} h^{-1}) reported by Chen *et al.*[18] Das *et al.* reported 0.35 μm-thick non-functionalised h-BN/PVDF membranes with flux rates of 1240 L m^{-2} h^{-1}.[46] Furthermore, the LDH/BNOx membranes reported here exhibit flow rates more than 230 times higher than commercially available NF270–400 membranes (7 L m^{-2} h^{-1} bar^{-1} or 23.8 L m^{-2} h^{-1} @ 3.4 bar).[47] The highly efficient flow rate reported here can be attributed to the larger pore size observed for LDH/BNOx membranes compared to their pristine BNOx counterparts, as discussed previously in Section 3.1.

3.3. Adsorption behaviour of LDH/BNOx nanocomposite membranes

An analysis of the adsorption behaviour of the nanocomposite membranes was conducted to better understand the membrane retention mechanism. UV-vis spectra showing the adsorption of each of the dyes over time can be found in Section S.4 of the ESI (Fig. S.12).† Adsorption of dyes on many nanomaterials, including both BN and LDH, is often best described by the PSO kinetic model.[48,49] Here, we observe two distinct adsorption behaviours in the case of these nanocomposite membranes, which are seemingly dependent on the charge of the dyes. The

anionic dyes (EB and MO) follow an expected PSO adsorption model, as shown in Fig. 6.

LDHs typically have a stronger adsorption capacity for anionic dyes due to attractive electrostatic interactions. However, here we observe the rate remaining constant over the experiment, whereas a change in rate would generally be expected as more LDH sites are occupied. This reaffirms the point that the π–π interactions between the BNOx and the dyes dominate over the electrostatic forces in the retention process, and serves as an explanation as to why there is no observable trend between the charge of the dyes and the retention of the membrane. However, for the cationic dyes, we see a deviation from simple PSO-type adsorption behaviour. The observed adsorption data can be split into two "stages" – stage I with fluctuating values and no clear correlation to the PSO model, and a stage II which fits to the PSO model. To gain further insight into this charge-dependent adsorption behaviour, the intra-particle diffusion (IPD) model was applied to the adsorption of all four dyes by the nanocomposite.[50,51] The parameters obtained from the PSO and IPD fitting are shown in Table 3.

For anionic dyes (EB and MO), the data is observed to fit the linear intra-particle diffusion model, with high R^2 values. According to the IPD model, if the straight line plot of q_t *vs.* $t^{0.5}$ does not pass through the origin, then IPD is not the rate limiting step.[52,53] It can be observed for all dyes that none of the lines pass through the origin, indicating another adsorption process occurring in conjunction with IPD. This is likely the π–π interactions previously discussed, as well as electrostatic interactions between the dyes and the nanocomposite. However, for the cationic dyes (MB and RhB), a multi-linear adsorption profile can be observed. This is particularly evident in the case of MB. It is once again clear that two distinct adsorption processes occur, denoted stages I and II. Stage I is a sharper region and represents rapid surface adsorption. Stage II can be characterised by a smaller slope and the slower diffusion of the dyes into the pores of the membrane. We propose that this two-stage process arises for adsorption of cationic dyes due to the composition of the nanocomposites. Zeta potential measurements of the LDH/BNOx nanocomposite indicate a partial negative surface charge ($\zeta_{LDH/BNOx} = -8.12$ mV) (Fig. S.3†). A larger proportion of partially negatively charged BNOx than LDH in the nanocomposite attracts the cationic dyes to the surface faster, followed by a slow diffusion into the pores and retention by π–π interactions, resulting in two distinct rates arising from the IPD model.

3.4. Photocatalytic degradation of dyes by LDH/BNOx nanocomposite membranes

The excellent retention values of these membranes are in line with our previous reports, as well as other reports for similar systems in literature, and present an efficient route to water purification. However, a main drawback of pristine BN and BNOx-based membranes is fouling. The adsorption of the aforementioned dyes by the membranes leads to saturation of the BNOx nanosheets, which in turn results in lower retention values over time, limiting their reusability. A potential method to overcome this is the integration of photocatalysts in these membranes. Transition metal-containing LDHs have been previously reported to be promising photocatalysts for a variety of reactions, including photodegradation of water soluble dyes.[54–56] Therefore it was decided to exploit this property, and test the anti-fouling capabilities of these LDH-containing membranes using a simple, low-cost household visible light source. 10 μL of 30% w/w H_2O_2 was used to boost the catalytic activity, the reasons for which will be discussed in Section 3.5.[57] The catalytic performance of the LDH/BNOx nanocomposite membranes for the degradation of EB, MB, MO and RhB was monitored using UV-visible spectroscopy. Fig. 7 shows the reduction in the maximum absorbances as a result of decolourisation of the solution due to degradation of each of the

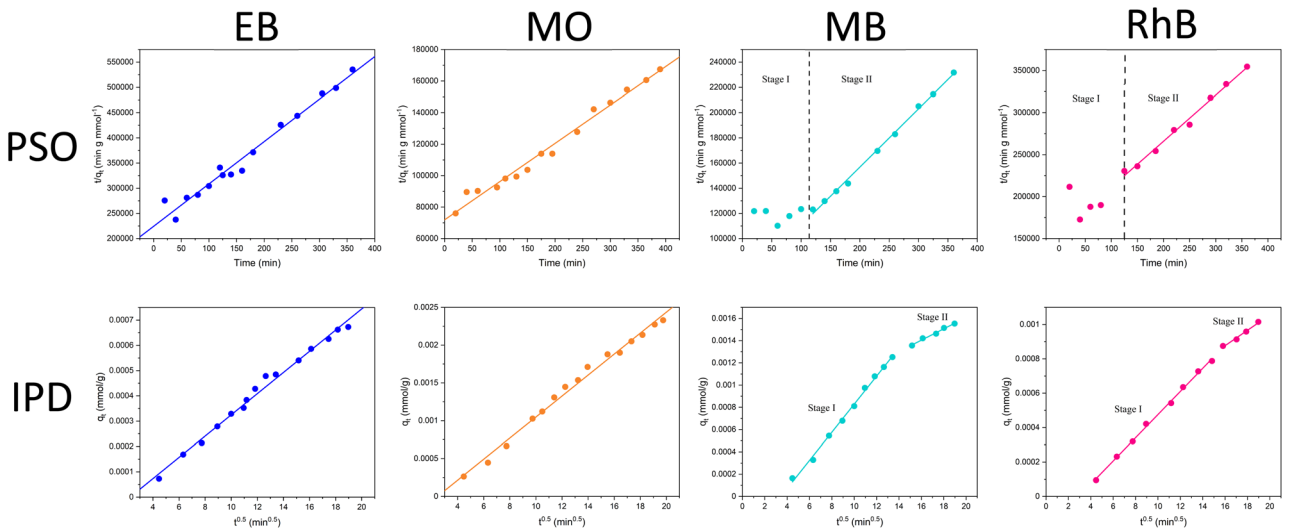

Fig. 6 (Top) Pseudo-second order and (bottom) intra-particle diffusion kinetic models for adsorption of dyes on to LDH/BNOx nanocomposite membranes.

Table 3 PSO and IPD parameters from fitting models to dye adsorption on LDH/BNOx nanocomposites

	PSO kinetics			IPD kinetics	
				$k_{IPD,1}$ (mmol g^{-1} min$^{-0.5}$)	$R_{IPD,1}^2$
Dye	k_2 (g mmol^{-1} min^{-1})	q_2 (mmol g^{-1})	R_2^2	$k_{IPD,2}$	$R_{IPD,2}^2$
Evans blue	3.156	0.0012	0.9748	4.193×10^{-5}	0.9901
				—	—
Methyl orange	0.823	0.0041	0.9843	1.389×10^{-4}	0.9909
				—	—
Methylene blue	3.339	0.0022	0.9972	1.262×10^{-4}	0.9964
				5.112×10^{-5}	0.9880
Rhodamine B	1.924	0.0018	0.9914	6.432×10^{-5}	0.9979
				4.448×10^{-5}	0.9841

dyes. It can be observed that each of the dyes is degraded significantly over a 120 minute time frame, with the best result being achieved for MB. It is also important to highlight the significance of the result of degradation of EB by these nanocomposites, as reports of the visible-light photodegradation of EB are difficult to find. To the best of our knowledge, this is the first report of EB degradation using a LDH photocatalyst.

Images of membrane samples after filtration and after photodegradation are shown in Fig. 8. The membranes can be seen to return completely to their original pale-blue colour after the photodegradation process. The dye photodegradation process was modelled by PFO kinetics, as described in Section 2.8 (eqn (4)). The best results for each of the dyes are presented here, however each experiment was conducted in triplicate – the results of the other runs are shown in Section S.5 of ESI (Fig. S.13 and Table S.4†). The kinetics of organic dye degradation is often best described by the Langmuir–Hinshelwood model, which at low dye concentrations – as we have here – can be simplified to a PFO model.[58] The apparent PFO rates for the best run of each dye are summarised in Fig. 7(e) and in Table 4. The PFO degradation rate constants obtained for the LDH/BNOx catalytic membrane compare favourably to similar systems reported in the literature. For example, a Co-based LDH synthesised in water, using 40 μL of H_2O_2 in the photodegradation process, had a calculated rate constant of 3.5×10^{-3} min^{-1} for degradation of RhB.[59] Nayak *et al.* synthesised MgCr LDH nanoplatelets for sunlight-driven degradation of RhB in the absence of H_2O_2, and calculated the rate constant to be 0.015 min^{-1}.[60] Although their light harvesting capabilities are superior, it is preferred to avoid the use of Cr-containing LDHs in water treatment applications if possible, as leaching of Cr^{3+} and Cr^{6+} is a potential hazard depending on the

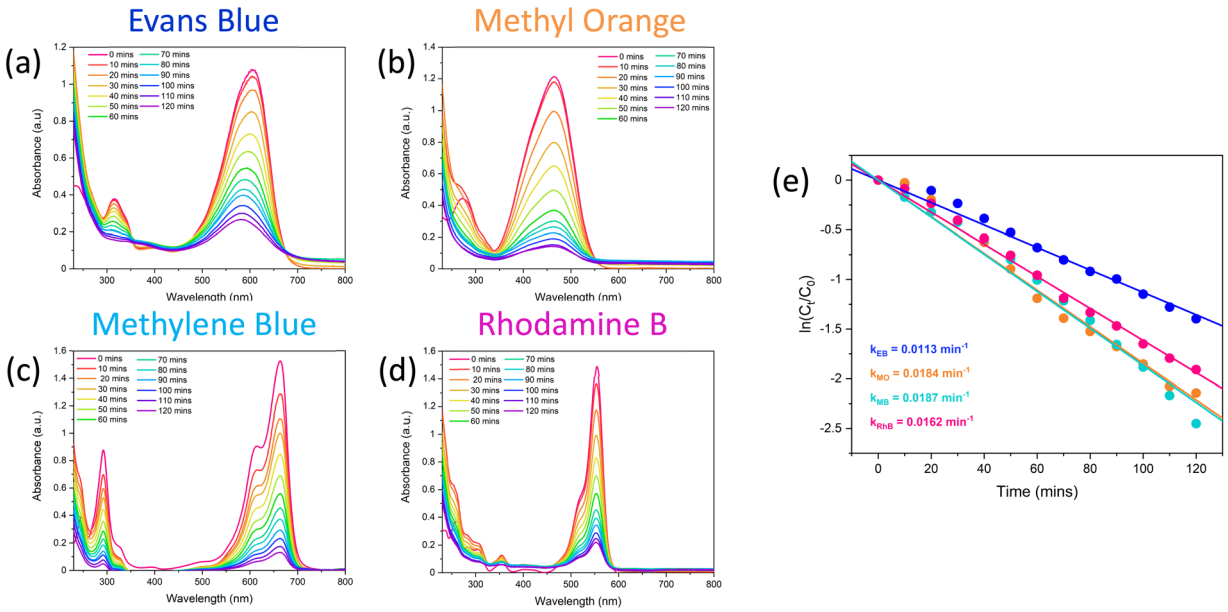

Fig. 7 Reduction in UV-vis absorbance of (a) Evans blue, (b) methyl orange, (c) methylene blue and (d) rhodamine B by visible-light photodegradation in the presence of LDH/BNOx membrane catalysts and 10 μL of H_2O_2 (30% w/w). (e) PFO models for degradation of Evans blue, methyl orange, methylene blue and rhodamine B.

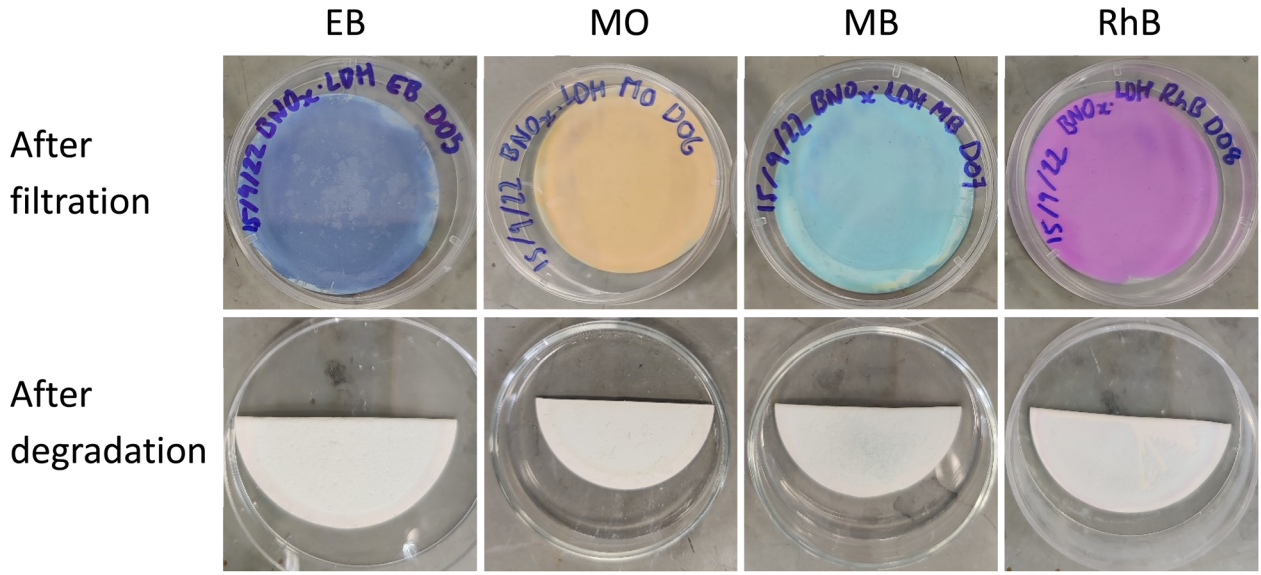

Fig. 8 Pictures of membranes before (top) and after (bottom) photodegradation using 10 μL H_2O_2 (30% w/w) and a 5 W COB LED.

conditions.[35] Ahmed *et al.* reported PFO rate constants of 0.01 min^{-1} for visible-light degradation of MO by NiAl LDH photocatalysts.[29] It is clear therefore that the LDH/BNOx membrane developed here is comparable with existing LDH-based photocatalysts for organic pollutant degradation.

Control experiments were conducted in the absence of catalyst, and showed insignificant extents of dye degradation in comparison with the photocatalytic nanocomposite membrane, and can be found in Section S.5 of ESI (Fig. S.14).† It is clear in the case of EB, MO and RhB that photolysis in the presence of H_2O_2 and the absence of catalyst is minimal. A non-negligible degree of photolysis was observed in the case of MB, where roughly 20% of the dye was degraded in the absence of catalyst in 120 minutes. However, this was to be expected, as aqueous solutions of methylene blue are prone to photobleaching in the presence of visible light.[61]

Nevertheless, the presence of the catalyst in this case clearly results in a more rapid degradation of the dye. While the removal of the dyes by photodegradation allows for the material to be reused, the membrane itself suffers from mechanical failure, due in part to the generation of gas bubbles under illumination (Fig. S.15†). SEM imaging of the membranes after photodegradation reveals exfoliation of the membranes, as well the generation of spherical cavities due to evolution of gases during the reaction (Fig. 9). Despite the excellent retention, flux, and catalytic activity of these membranes, it is evident that further research is needed to address the mechanical integrity and ensure the device itself is reusable – not just the material it consists of. Chemical cross-linking of the nanosheets within the membrane would be the ideal next step to address the issues with mechanical stability. Nevertheless, the efficient and rapid visible-light photodegradation of the dyes in these high-retention, high-flux membranes is an exciting and promising result in the search for efficient NF membranes that are resistant to fouling.

3.5. Proposed photodegradation mechanism

Bulk h-BN is an indirect wide bandgap semiconductor, with reported bandgap values in the deep UV (~6 eV).[62] While an indirect-to-direct bandgap transition has been theorised on reducing the thickness of h-BN from few-layer to monolayer, the band-gap value remains large (6.46 eV). Photocatalysis has been observed in BN, however it is achieved through introduction of defects, and using UVC illumination.[63] For these reasons, it is unlikely that there is any significant contribution from BNOx to the visible-light photocatalytic activity observed in this study. The source of photocatalytic degradation can be primarily assigned to the presence of CuAl–CO_3 LDH in the nanocomposite in this case.

Table 4 Degradation extents at $t = 120$ min, and PFO model rate constants for degradation of dyes by LDH/BNOx nanocomposite membranes

Dye	Highest degradation at 120 min (%)	Highest k_1 (min^{-1})	R_1^2	Average k_1 (min^{-1})
Evans blue	75	0.0113	0.9950	0.0091 ± 0.0019
Methyl orange	88	0.0184	0.9949	0.0131 ± 0.0040
Methylene blue	91	0.0187	0.9934	0.0174 ± 0.0021
Rhodamine B	85	0.0162	0.9980	0.0151 ± 0.0008

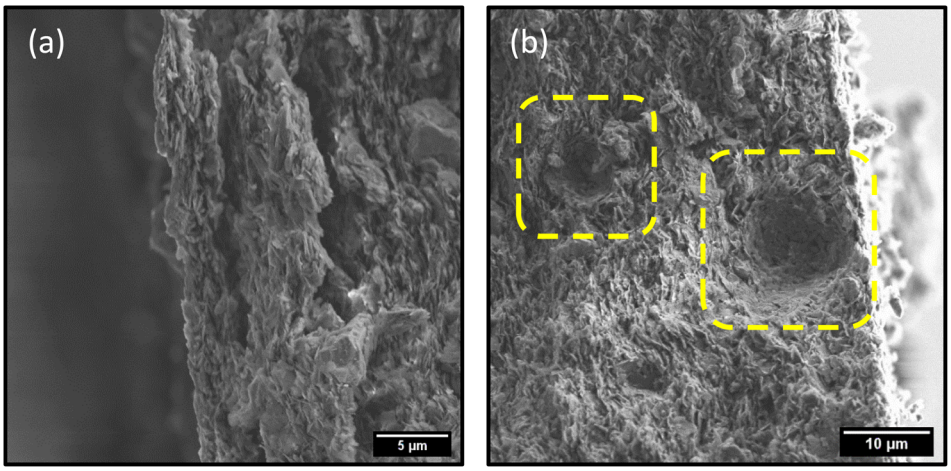

Fig. 9 SEM images depicting (a) exfoliation of membrane and (b) formation of micro-bubble shaped cavities in membrane during photo-degradation process.

UV-vis absorption spectra of LDHs can provide key information on their suitability as visible light photocatalysts.[25] Due to the intense light scattering exhibited by 2D nanosheets in solution, it is necessary to carry out the UV-vis in solid state using DR UV-vis to identify the key absorption features.[64] The DR UV-vis spectrum of CuAl–CO_3 LDHs reveals two main absorption features – the first centred around 475 nm, which can be attributed to O^{2-} to Cu^{2+} ligand to metal charge transfer, and the second at 700 nm, associated with Cu^{2+} d–d transitions (Fig. S.16†).[65,66] These significant absorption features in the visible region indicate the CuAl–CO_3 LDH is a good candidate for visible-light photocatalysis.

As LDHs function as doped semiconductors, photocatalysis in LDHs is commonly accepted to be due to formation of electron–hole pairs as a result of light absorption. This behaviour has been well described by Baliarsingh *et al.*, as well as Xia *et al.* for a variety of LDHs, and we propose a similar mechanism for our system.[54,67] Photogenerated holes (h^+) react with water in the aqueous dye solution to form hydroxyl radicals ($\cdot OH$). The photoexcited electrons (e^-) react with oxygen adsorbed on the LDH surface from dissolved oxygen in solution, forming superoxide radicals ($O_2^{\cdot -}$) (eqn (6) and (7)).

$$h^+ + H_2O \rightarrow 2H^+ + 2\cdot OH \quad (6)$$

$$e^- + O_2 \rightarrow O_2^{\cdot -} \quad (7)$$

$O_2^{\cdot -}$ radicals can be protonated to form hydroperoxyl radicals ($HO_2^{\cdot}$). H_2O_2 is generated by the formation and combination of $HO_2^{\cdot}$ radicals. The reaction between photoexcited electrons and H_2O_2 produces more $\cdot OH$ radicals which, along with $O_2^{\cdot -}$, are reactive oxygen species, resulting in degradation of the dyes (eqn (8)–(10)).[54]

$$O_2^{\cdot -} + H^+ \rightarrow HO_2^{\cdot} \quad (8)$$

$$2HO_2^{\cdot} \rightarrow H_2O_2 + O_2 \quad (9)$$

$$H_2O_2 + e^- \rightarrow \cdot OH + OH^- \quad (10)$$

Apparent photocatalysis reaction rates in LDHs are limited by both electron–hole pair generation, as well as separation and carrier mobilities.[55,68] CO_3^{2-} intercalation in LDHs is reported to suppress the electron–hole recombination to an extent, thus increasing the apparent reaction rates, however high rates of degradation of dyes under visible-light illumination by pristine binary LDHs, particularly CuAl LDHs, is still rarely reported.[54,69] To overcome this hurdle, small amounts of H_2O_2 were added to the solution, much less than previous reports for similar systems.[70] The addition of H_2O_2 to Cu^{2+}-based photocatalytic systems may improve the photocatalytic performance *via* two routes. Firstly, H_2O_2 acts as an electron acceptor, reducing the electron–hole recombination rate, thus enhancing the visible-light-driven generation of $\cdot OH$ and $O_2^{\cdot -}$. Secondly, Cu^{2+}-containing solids can also drive the catalytic decomposition of H_2O_2 to generate $\cdot OH$ radicals *via* Fenton-like redox processes (eqn (11) and (12)).[71,72]

$$Cu^{2+} + H_2O_2 \rightarrow Cu^+ + HO_2^{\cdot} + OH^- \quad (11)$$

$$Cu^+ + H_2O_2 \rightarrow Cu^{2+} + \cdot OH + OH^- \quad (12)$$

In this system, much lower rates of degradation are observed in the absence of H_2O_2. This was demonstrated using RhB in Section S.5 of ESI (Fig. S.17)† where 58% of RhB is seen to be removed from solution after 120 minutes, compared to 85% removal upon addition of H_2O_2. Furthermore, it is difficult to separate the contributions of adsorption and photodegradation processes in the absence of H_2O_2, as roughly 45% of RhB is adsorbed at that same point in time in dark conditions. To gain insights into the catalytic mechanism, the terephthalic acid (TA) probe technique was used to monitor the formation of $\cdot OH$ radicals. TA is a highly sensitive $\cdot OH$ radical probe, reacting to form a fluorescent product – hydroxyterephthalic acid (hTA), which can be monitored using photoluminescence

spectroscopy (PL).[33,73] Under excitation with 315 nm light, hTA has a characteristic emission band centred around 420 nm, and the intensity of this emission band while used in this context in photocatalytic systems is representative of more efficient generation of ·OH radicals. PL emission spectra were recorded for four different environments – TA + LDH/BNOx + dark, TA + LDH/BNOx + dark + H_2O_2, TA + LDH/BNOx + light, and TA + LDH/BNOx + light + H_2O_2, as shown in Fig. 10.

It can be observed that in the absence of light and H_2O_2, there is no measurable emission that is characteristic of the presence of hTA, meaning there is minimal ·OH radical generation in these conditions. Upon addition of H_2O_2, the appearance of a significant emission peak can be observed in dark conditions, confirming that the LDH/BNOx acts as a Fenton-type catalyst. Exposure to light in the absence of H_2O_2 results in the generation of a low intensity emission peak, which is to be expected, as generation of ·OH radicals by LDHs is limited by electron–hole recombination. The most intense signal is observed when the LDH/BNOx catalyst is exposed to light in the presence of H_2O_2, resulting in the formation of more ·OH radicals through both Fenton-type reactions, as well as from photoexcited electrons and photogenerated holes. Based on these experimental observations, we propose that the catalytic mechanism is a synergistic process, with contributions from Cu^{2+}-based photo-Fenton-type chemistry, as well as the semiconducting behaviour of CuAl–CO_3 LDHs.

·OH radicals are expected to initiate degradation of these dyes by disrupting the chromophores, *via* azo bond cleavage in EB and MO, and ring opening mechanisms in the case of RhB and MB. UV-vis provides indirect evidence of this proposal in the case of EB – a diazo dye – as a decrease in UV-vis absorbance intensity is accompanied by a significant blue shift λ_{max} from 608 nm to 580 nm (Fig. 7(a)). This is indicative of a reduction in the extent of conjugation due to reduction and subsequent cleavage of the azo bond.[74] Tentative proposed mechanisms of the initial steps of degradation of each of the dyes are shown in Fig. 11, based on experimental observations for EB, as well as evidence in the literature for similar systems for degradation of the other dyes.[75–78]

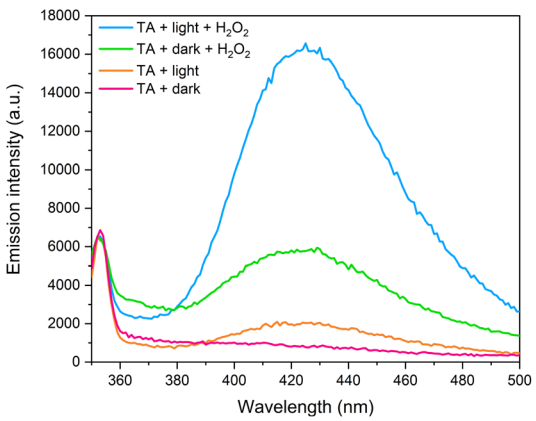

Fig. 10 Photoluminescence emission spectra of hydroxyterephthalic acid generated using LDH/BNOx catalyst.

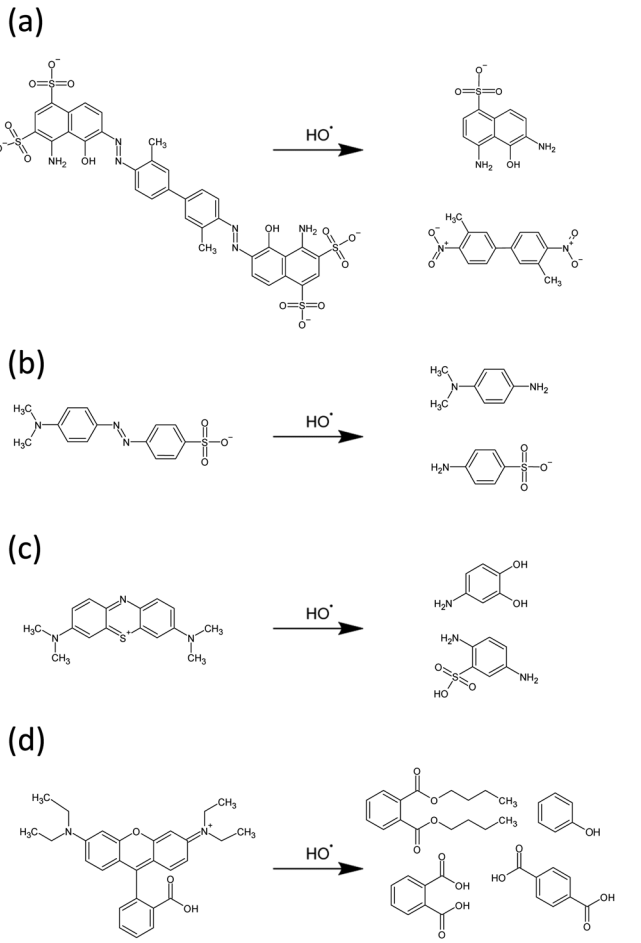

Fig. 11 Proposed mechanisms of initial degradation steps of (a) EB, (b) MO, (c) MB and (d) RhB by hydroxyl radicals.

4 Conclusions

Thus, we have developed novel LDH/BNOx nanocomposite membranes for advanced NF applications. The membranes have been produced using multiple processing steps, including co-precipitation, liquid-phase exfoliation, and vacuum filtration techniques. The excellent NF performance of these membranes was demonstrated, with up to 100% dye retention being achieved. The dye retention and solvent flux results are in line with some of the best reported to date. Furthermore, the membranes have demonstrated excellent photocatalytic degradation and removal of dyes under visible-light ambient conditions. This approach should enable us to address the critical membrane fouling problem, allowing for regeneration and re-use of the membranes. However, currently our membranes are fragile and require the presence of the Durapore membrane filter template as a substrate for mechanical stability. Our future work will involve the improvement of the mechanical stability of membranes by chemical cross-linking of the nanosheets to produce membranes with higher mechanical integrity. Nevertheless, we believe this work represents a significant step forward in advanced nanofiltration technology.

Author contributions

Conceptualisation: Y. K. G., Á. C. and N. G. D.; methodology: Y. K. G., Á. C., N. G. D. and D. M. G.; formal analysis: Á. C., N. G. D., D. M. G., T. S., A. R. and A. D.; investigation: Á. C., N. G. D., D. M. G., T. S., A. R. Q. F. and A. D.; resources: Y. K. G.; data curation: Á. C., N. G. D., D. M. G. and T. S.; writing – original draft preparation: Á. C., D. M. G. and Y. K. G.; writing – review and editing: Á. C., N. G. D., D. M. G., T. S., A. R. and Y. K. G.; supervision: Á. C. and Y. K. G.; project administration: Y. K. G.; funding acquisition: Á. C. and Y. K. G.

Conflicts of interest

There are no conflicts to declare.

Acknowledgements

Á. C. and Y. K. G. acknowledge support from the Irish Research Council (grant number: GOIPG/2019/2788). N. G. D. and Y. K. G. acknowledge support from Science Foundation Ireland (SFI) and BiOrbic Bioeconomy Research Centre (grant number: SFI 16/RC/3889). T. S. and V. N. acknowledge support from the SFI Centre for Doctoral Training in Advanced Characterisation of Materials (CDT-ACM) (SFI Award Reference 18/EPSRC-CDT/3581). The authors also wish to thank the Advanced Microscopy Laboratory, Trinity College Dublin for their technical support and the use of their facilities.

References

1 *Progress on Household Drinking Water, Sanitation and Hygiene I 2000–2017*, New York, 2019.
2 R. Kishor, D. Purchase, G. D. Saratale, R. G. Saratale, L. F. R. Ferreira, M. Bilal, R. Chandra and R. N. Bharagava, Ecotoxicological and health concerns of persistent coloring pollutants of textile industry wastewater and treatment approaches for environmental safety, *J. Environ. Chem. Eng.*, 2021, **9**, 105012.
3 M. Imran, D. E. Crowley, A. Khalid, S. Hussain, M. W. Mumtaz and M. Arshad, Microbial biotechnology for decolorization of textile wastewaters, *Rev. Environ. Sci. Biotechnol.*, 2015, **14**, 73–92.
4 J. Khatri, P. V. Nidheesh, T. S. A. Singh and M. S. Kumar, Advanced oxidation processes based on zero-valent aluminium for treating textile wastewater, *Chem. Eng. J.*, 2018, **348**, 67–73.
5 G. McMullan, C. Meehan, A. Conneely, N. Kirby, T. Robinson, P. Nigam, I. M. Banat, R. Marchant and W. F. Smyth, Microbial decolourisation and degradation of textile dyes, *Appl. Microbiol. Biotechnol.*, 2001, **56**, 81–87.
6 B. Lellis, C. Z. Fávaro-Polonio, J. A. Pamphile and J. C. Polonio, Effects of textile dyes on health and the environment and bioremediation potential of living organisms, *Biotechnol. Res. Innov.*, 2019, **3**, 275–290.
7 M. N. Morshed, S. Al Azad, H. Deb, B. B. Shaun and X. L. Shen, Titania-loaded cellulose-based functional hybrid nanomaterial for photocatalytic degradation of toxic aromatic dye in water, *J. Water Process Eng.*, 2020, **33**, 101062.
8 S. Srivastava, R. Sinha and D. Roy, Toxicological effects of malachite green, *Aquat. Toxicol.*, 2004, **66**, 319–329.
9 N. G. Doménech, F. Purcell-Milton and Y. K. Gun'ko, Recent progress and future prospects in development of advanced materials for nanofiltration, *Mater. Today Commun.*, 2020, **23**, 100888.
10 N. G. Doménech, F. Purcell-Milton, A. S. Arjona, M.-L. C. García, M. Ward, M. B. Cabré, A. Rafferty, K. McKelvey, P. Dunne and Y. K. Gun'ko, High-Performance Boron Nitride-Based Membranes for Water Purification, *Nanomaterials*, 2022, **12**, 473.
11 E. M. Vrijenhoek, S. Hong and M. Elimelech, Influence of membrane surface properties on initial rate of colloidal fouling of reverse osmosis and nanofiltration membranes, *J. Membr. Sci.*, 2001, **188**, 115–128.
12 L. Yang, X. Zhang, J. Rahmatinejad, B. Raisi and Z. Ye, Triethanolamine-based zwitterionic polyester thin-film composite nanofiltration membranes with excellent fouling-resistance for efficient dye and antibiotic separation, *J. Membr. Sci.*, 2023, **670**, 121355.
13 J. H. Jhaveri and Z. V. P. Murthy, A comprehensive review on anti-fouling nanocomposite membranes for pressure driven membrane separation processes, *Desalination*, 2016, **379**, 137–154.
14 X. Chen, M. Qiu, H. Ding, K. Fu and Y. Fan, A reduced graphene oxide nanofiltration membrane intercalated by well-dispersed carbon nanotubes for drinking water purification, *Nanoscale*, 2016, **8**, 5696–5705.
15 L. Sun, H. Huang and X. Peng, Laminar MoS2 membranes for molecule separation, *Chem. Commun.*, 2013, **49**, 10718–10720.
16 Á. Coogan and Y. K. Gun'ko, Solution-based "bottom-up" synthesis of group VI transition metal dichalcogenides and their applications, *Mater. Adv.*, 2021, **2**, 146–164.
17 S. Homaeigohar and M. Elbahri, Graphene membranes for water desalination, *NPG Asia Mater.*, 2017, **98**(9), e427.
18 C. Chen, J. Wang, D. Liu, C. Yang, Y. Liu, R. S. Ruoff and W. Lei, Functionalized boron nitride membranes with ultrafast solvent transport performance for molecular separation, *Nat. Commun.*, 2018, **91**(9), 1–8.
19 J. Fatima, A. N. Shah, M. B. Tahir, T. Mehmood, A. A. Shah, M. Tanveer, R. Nazir, B. L. Jan and S. Alansi, Tunable 2D Nanomaterials; Their Key Roles and Mechanisms in Water Purification and Monitoring, *Front. Environ. Sci.*, 2022, **10**, 210.
20 J. Zhang, Z. Li, K. Zhan, R. Sun, Z. Sheng, M. Wang, S. Wang and X. Hou, Two dimensional nanomaterial-based separation membranes, *Electrophoresis*, 2019, **40**, 2029–2040.
21 N. G. Doménech, Á. Coogan, F. Purcell-Milton, M. L. C. García, A. S. Arjona, M. B. Cabré, A. Rafferty, K. Mckelvey, P. W. Dunne and Y. K. Gun'ko, Partially oxidised boron nitride as a 2D nanomaterial for nanofiltration applications, *Nanoscale Adv.*, 2022, **4**, 4895–4904.

22 Y. Andriani, J. Song, P. C. Lim, D. H. L. Seng, D. M. Y. Lai, S. L. Teo, J. Kong, X. Wang, X. Zhang and S. Liu, Green and efficient production of boron nitride nanosheets via oxygen doping-facilitated liquid exfoliation, *Ceram. Int.*, 2019, **45**, 4909–4917.
23 Q. Wang and D. Ohare, Recent advances in the synthesis and application of layered double hydroxide (LDH) nanosheets, *Chem. Rev.*, 2012, **112**, 4124–4155.
24 G. Arrabito, A. Bonasera, G. Prestopino, A. Orsini, A. Mattoccia, E. Martinelli, B. Pignataro and P. G. Medaglia, Layered Double Hydroxides: A Toolbox for Chemistry and Biology, *Crystals*, 2019, **9**, 361.
25 C. G. Silva, Y. Bouizi, V. Fornés and H. García, Layered double hydroxides as highly efficient photocatalysts for visible light oxygen generation from water, *J. Am. Chem. Soc.*, 2009, **131**, 13833–13839.
26 J. Yu, F. Yu, M. F. Yuen and C. Wang, Two-dimensional layered double hydroxides as a platform for electrocatalytic oxygen evolution, *J. Mater. Chem. A*, 2021, **9**, 9389–9430.
27 C. Hobbs, S. Jaskaniec, E. K. McCarthy, C. Downing, K. Opelt, K. Güth, A. Shmeliov, M. C. D. Mourad, K. Mandel and V. Nicolosi, Structural transformation of layered double hydroxides: an in situ TEM analysis, *npj 2D Mater. Appl.*, 2018, **2**, 1–10.
28 P. Miao, J. Zhao, R. Shi, Z. Li, Y. Zhao, C. Zhou and T. Zhang, Layered Double Hydroxide Engineering for the Photocatalytic Conversion of Inactive Carbon and Nitrogen Molecules, *ACS ES&T Engg*, 2022, **2**, 1088–1102.
29 M. S. Ahmed, M. S. J. Khan, S. B. Khan, K. Akhtar, E. M. Bakhsh, A. Khalil, S. A. Khan, A. M. Asiri and T. Kamal, Ni–Al-layered double-hydroxide photocatalyst for the visible light-assisted photodegradation of organic dye pollutants, *Appl. Nanosci.*, 2022, **12**, 3597–3606.
30 D. Saliba, S. E. El Jamal, A. Jonderian, M. Ammar, M. Hmadeh and M. Al-Ghoul, Tuning the structural properties of cadmium–aluminum layered double hydroxide for enhanced photocatalytic dye degradation, *RSC Adv.*, 2020, **10**, 43066–43074.
31 S. Berner, P. Araya, J. Govan and H. Palza, Cu/Al and Cu/Cr based layered double hydroxide nanoparticles as adsorption materials for water treatment, *J. Ind. Eng. Chem.*, 2018, **59**, 134–140.
32 Á. Coogan, L. Hughes, F. Purcell-Milton, S. Cardiff, V. Nicolosi and Y. K. Gun'ko, Two-Dimensional Chiroptically Active Copper Oxide Nanostructures, *J. Phys. Chem. C*, 2022, **126**, 18980–18987.
33 S. E. Page, W. A. Arnold and K. McNeill, Terephthalate as a probe for photochemically generated hydroxyl radical, *J. Environ. Monit.*, 2010, **12**, 1658–1665.
34 C. Wei, X. Yan, Y. Zhou, W. Xu, Y. Gan, Y. Zhang and N. Zhang, Morphological Control of Layered Double Hydroxides Prepared by Co-Precipitation Method, *Crystals*, 2022, **12**, 1713.
35 A. V. Radha and P. V. Kamath, Oxidative leaching of chromium from layered double hydroxides: mechanistic studies, *Bull. Mater. Sci.*, 2004, **27**, 355–360.
36 T. Tanaka, Y. Kameshima, S. Nishimoto and M. Miyake, Determination of carbonate ion contents in layered double hydroxides by FTIR spectrometry, *Anal. Methods*, 2012, **4**, 3925–3927.
37 C. Backes, B. M. Szydłowska, A. Harvey, S. Yuan, V. Vega-Mayoral, B. R. Davies, P. L. Zhao, D. Hanlon, E. J. G. Santos, M. I. Katsnelson, W. J. Blau, C. Gadermaier and J. N. Coleman, Production of highly monolayer enriched dispersions of liquid-exfoliated nanosheets by liquid cascade centrifugation, *ACS Nano*, 2016, **10**, 1589–1601.
38 M. Xu, Q. Tang, Y. Liu, J. Shi, W. Zhang, C. Guo, Q. Liu, W. Lei and C. Chen, Charged Boron Nitride Nanosheet Membranes for Improved Organic Solvent Nanofiltration, *ACS Appl. Mater. Interfaces*, 2023, **15**, 12524–12533.
39 M. Sajid, S. M. S. Jillani, N. Baig and K. Alhooshani, Layered double hydroxide-modified membranes for water treatment: recent advances and prospects, *Chemosphere*, 2022, **287**, 132140.
40 H. Jee, J. Jang, Y. Kang, T. Eisa, K. J. Chae, I. S. Kim and E. Yang, Enhancing the Dye-Rejection Efficiencies and Stability of Graphene Oxide-Based Nanofiltration Membranes via Divalent Cation Intercalation and Mild Reduction, *Membranes*, 2022, **12**, 402.
41 L. Sun, Y. Ying, H. Huang, Z. Song, Y. Mao, Z. Xu and X. Peng, Ultrafast molecule separation through layered WS2 nanosheet membranes, *ACS Nano*, 2014, **8**, 6304–6311.
42 G. Darmograi, B. Prelot, G. Layrac, D. Tichit, G. Martin-Gassin, F. Salles and J. Zajac, Study of Adsorption and Intercalation of Orange-Type Dyes into Mg-Al Layered Double Hydroxide, *J. Phys. Chem. C*, 2015, **119**, 23388–23397.
43 R. Sasai, H. Sato, M. Sugata, T. Fujimura, S. Ishihara, K. Deguchi, S. Ohki, M. Tansho, T. Shimizu, N. Oita, M. Numoto, Y. Fujii, S. Kawaguchi, Y. Matsuoka, K. Hagura, T. Abe and C. Moriyoshi, Why Do Carbonate Anions Have Extremely High Stability in the Interlayer Space of Layered Double Hydroxides? Case Study of Layered Double Hydroxide Consisting of Mg and Al (Mg/Al = 2), *Inorg. Chem.*, 2019, **58**, 10928–10935.
44 I. Itskou, A. L'Hermitte, S. Marchesini, T. Tian and C. Petit, How to Tailor Porous Boron Nitride Properties for Applications in Interfacial Processes, *Acc. Mater. Res.*, 2023, **4**, 143–155.
45 T. Chen, M. Li and J. Liu, π-π Stacking Interaction: A Nondestructive and Facile Means in Material Engineering for Bioapplications, *Cryst. Growth Des.*, 2018, **18**, 2765–2783.
46 R. Das, P. Solís-Fernández, D. Breite, A. Prager, A. Lotnyk, A. Schulze and H. Ago, High flux and adsorption based non-functionalized hexagonal boron nitride lamellar membrane for ultrafast water purification, *Chem. Eng. J.*, 2021, **420**, 127721.
47 *Nanofiltration (NF)*, **https://www.dupont.com/water/technologies/nanofiltration-nf.html**, accessed, 2 May 2023.
48 R. S. Bangari, A. Yadav, P. Awasthi and N. Sinha, Experimental and theoretical analysis of simultaneous removal of methylene blue and tetracycline using boron

nitride nanosheets as adsorbent, *Colloids Surf., A*, 2022, **634**, 127943.
49 G. Rathee, A. Awasthi, D. Sood, R. Tomar, V. Tomar and R. Chandra, A new biocompatible ternary Layered Double Hydroxide Adsorbent for ultrafast removal of anionic organic dyes, *Sci. Rep.*, 2019, **91**(9), 1–14.
50 W. J. Weber Jr and J. C. Morris, Kinetics of Adsorption on Carbon from Solution, *J. Sanit. Eng. Div.*, 1963, **89**, 31–59.
51 T. Sekine and K. Nakatani, Intraparticle diffusion and adsorption isotherm for sorption in silica gel studied by single-microparticle injection and microabsorption methods, *Langmuir*, 2002, **18**, 694–697.
52 T. Hou, H. Zhang, D. He, Q. Liu, Z. Zhang, L. Xiao, W. Li and M. Barnes, Enhanced adsorption behaviors of Co2+ on robust chitosan hydrogel microspheres derived from an alkali solution system: kinetics and isotherm analysis, *RSC Adv.*, 2018, **8**, 36858–36868.
53 A. Pholosi, E. B. Naidoo and A. E. Ofomaja, Intraparticle diffusion of Cr(VI) through biomass and magnetite coated biomass: a comparative kinetic and diffusion study, *S. Afr. J. Chem. Eng.*, 2020, **32**, 39–55.
54 N. Baliarsingh, K. M. Parida and G. C. Pradhan, Effects of Co, Ni, Cu, and Zn on photophysical and photocatalytic properties of carbonate intercalated MII/Cr LDHs for enhanced photodegradation of methyl orange, *Ind. Eng. Chem. Res.*, 2014, **53**, 3834–3841.
55 L. Mohapatra and K. Parida, A review on the recent progress, challenges and perspective of layered double hydroxides as promising photocatalysts, *J. Mater. Chem. A*, 2016, **4**, 10744–10766.
56 N. Ahmed, Y. Shibata, T. Taniguchi and Y. Izumi, Photocatalytic conversion of carbon dioxide into methanol using zinc–copper–M(III) (M = aluminum, gallium) layered double hydroxides, *J. Catal.*, 2011, **279**, 123–135.
57 X. Yuan and W. Li, Graphitic-C3N4 modified ZnAl-layered double hydroxides for enhanced photocatalytic removal of organic dye, *Appl. Clay Sci.*, 2017, **138**, 107–113.
58 K. Abderrazek, F. S. Najoua and E. Srasra, Synthesis and characterization of [Zn–Al] LDH: study of the effect of calcination on the photocatalytic activity, *Appl. Clay Sci.*, 2016, **119**, 229–235.
59 H. Fazal, A. Iqbal, Y. Cao, J. Zai, N. Ali, Y. Zhang, X. Wu, X. Zhang and X. Qian, Porous urchin-like 3D Co(II)Co(III) layered double hydroxides for high performance heterogeneous Fenton degradation, *CrystEngComm*, 2021, **23**, 1234–1242.
60 S. Nayak, K. Parida and O. D. Pavel, MgCr-LDH Nanoplatelets as Effective Oxidation Catalysts for Visible Light-Triggered Rhodamine B Degradation, *Catalysts*, 2021, **11**, 1072.
61 S. J. M. Nassar, C. Wills and A. Harriman, Inhibition of the Photobleaching of Methylene Blue by Association with Urea, *ChemPhotoChem*, 2019, **3**, 1042–1049.
62 G. Cassabois, P. Valvin and B. Gil, Hexagonal boron nitride is an indirect bandgap semiconductor, *Nat. Photonics*, 2016, **104**(10), 262–266.
63 L. Duan, B. Wang, K. Heck, S. Guo, C. A. Clark, J. Arredondo, M. Wang, T. P. Senftle, P. Westerhoff, X. Wen, Y. Song and M. S. Wong, Efficient Photocatalytic PFOA Degradation over Boron Nitride, *Environ. Sci. Technol. Lett.*, 2020, **7**, 613–619.
64 A. Harvey, C. Backes, J. B. Boland, X. He, A. Griffin, B. Szydlowska, C. Gabbett, J. F. Donegan and J. N. Coleman, Non-resonant light scattering in dispersions of 2D nanosheets, *Nat. Commun.*, 2018, **91**(9), 1–11.
65 S. Velu, K. Suzuki, M. Okazaki, M. P. Kapoor, T. Osaki and F. Ohashi, Oxidative Steam Reforming of Methanol over CuZnAl(Zr)-Oxide Catalysts for the Selective Production of Hydrogen for Fuel Cells: Catalyst Characterization and Performance Evaluation, *J. Catal.*, 2000, **194**, 373–384.
66 S. Velu, K. Suzuki, S. Hashimoto, N. Satoh, F. Ohashi and S. Tomura, The effect of cobalt on the structural properties and reducibility of CuCoZnAl layered double hydroxides and their thermally derived mixed oxides, *J. Mater. Chem.*, 2001, **11**, 2049–2060.
67 S. J. Xia, F. X. Liu, Z. M. Ni, J. L. Xue and P. P. Qian, Layered double hydroxides as efficient photocatalysts for visible-light degradation of Rhodamine B, *J. Colloid Interface Sci.*, 2013, **405**, 195–200.
68 Z. R. Chen, Y. Q. Zhu, S. M. Xu, Y. Zhao, Q. Peng and H. Yan, Theoretical study on the anisotropic photo-induced carrier mobilities in layered double hydroxide-based photocatalysts, *J. Mater. Chem. A*, 2021, **9**, 20466–20482.
69 T. E. Eriksen, J. Lind and G. Merényi, On the acid-base equilibrium of the carbonate radical, *Radiat. Phys. Chem.*, 1985, **26**, 197–199.
70 J. Li, S. Zhang, Y. Chen, T. Liu, C. Liu, X. Zhang, M. Yi, Z. Chu and X. Han, A novel three-dimensional hierarchical CuAl layered double hydroxide with excellent catalytic activity for degradation of methyl orange, *RSC Adv.*, 2017, **7**, 29051–29057.
71 Z. Z. Yang, C. Zhang, G. M. Zeng, X. F. Tan, H. Wang, D. L. Huang, K. H. Yang, J. J. Wei, C. Ma and K. Nie, Design and engineering of layered double hydroxide based catalysts for water depollution by advanced oxidation processes: a review, *J. Mater. Chem. A*, 2020, **8**, 4141–4173.
72 A. D. Bokare and W. Choi, Review of iron-free Fenton-like systems for activating H2O2 in advanced oxidation processes, *J. Hazard. Mater.*, 2014, **275**, 121–135.
73 M. Myilsamy, M. Mahalakshmi, V. Murugesan and N. Subha, Enhanced photocatalytic activity of nitrogen and indium co-doped mesoporous TiO2 nanocomposites for the degradation of 2,4-dinitrophenol under visible light, *Appl. Surf. Sci.*, 2015, **342**, 1–10.
74 K. T. Chung, The significance of azo-reduction in the mutagenesis and carcinogenesis of azo dyes, *Mutat. Res., Genet. Toxicol.*, 1983, **114**, 269–281.
75 R. T. Kapoor, M. Danish, R. S. Singh, M. Rafatullah and A. K. Abdul, Exploiting microbial biomass in treating azo dyes contaminated wastewater: mechanism of degradation and factors affecting microbial efficiency, *J. Water Process Eng.*, 2021, **43**, 102255.

76 S. Wang, Y. Jia, L. Song and H. Zhang, Decolorization and Mineralization of Rhodamine B in Aqueous Solution with a Triple System of Cerium(IV)/H2O2/Hydroxylamine, *ACS Omega*, 2018, **3**, 18456–18465.

77 Q. Wang, S. Tian and P. Ning, Degradation mechanism of methylene blue in a heterogeneous fenton-like reaction catalyzed by ferrocene, *Ind. Eng. Chem. Res.*, 2014, **53**, 643–649.

78 V. S. Antonin, S. Garcia-Segura, M. C. Santos and E. Brillas, Degradation of Evans Blue diazo dye by electrochemical processes based on Fenton's reaction chemistry, *J. Electroanal. Chem.*, 2015, **747**, 1–11.